



Processing of high-strength thermal-resistant Al-2.2% cerium-1.3% lanthanum alloy rods with high electric conductivity by High Pressure Torsion Extrusion

Rui Xu^{1,2,3}, Yemao Lu^{1,3,*}, Yuting Dai^{1,2,3}, Andrea Brognara⁴, Horst Hahn^{1,2,5}, and Yulia Ivanisenko^{1,*} 

¹ Institute of Nanotechnology (INT), Karlsruhe Institute of Technology (KIT), Kaiserstr. 12, 76131 Karlsruhe, Germany

² Joint Research Laboratory Nanomaterials, Technical University of Darmstadt (TUDa), 64287 Darmstadt, Germany

³ Karlsruhe Nano Micro Facility (KNMFi), Karlsruhe Institute of Technology (KIT), 76344 Eggenstein-Leopoldshafen, Germany

⁴ Department of Structure and Nano-/Micromechanics of Materials, Max-Planck-Institut für Eisenforschung GmbH (MPIE), Max-Planck-Straße 1, 40237 Düsseldorf, Germany

⁵ School of Sustainable Chemical, Biological and Materials Engineering, The University of Oklahoma, Norman 73019, USA

Received: 31 January 2024

Accepted: 24 April 2024

© The Author(s), 2024

ABSTRACT

A novel severe plastic deformation (SPD) process of High Pressure Torsion Extrusion (HPTE) was applied to the rods of the Al-2.2 wt.% Ce-1.3 wt.% La (Al-3.5RE) alloy. The microstructure, microhardness, the mechanical strength, thermal stability, and electrical conductivity of the alloy after HPTE and subsequent annealing have been investigated. It was demonstrated that HPTE processing can simultaneously increase yield strength from 127 to 225 MPa and electrical conductivity from 54.7% IACS to 55.7% IACS in this alloy. Such a remarkable combination of properties was achieved thanks to significant refinement of microstructure constituents: grain size of Al matrix was reduced down to 0.9 μm and initially continuous network of $\text{Al}_{11}\text{RE}_3$ phase was broken to micrometer- and nanometer-sized particles. Furthermore, the yield strength of the HPTE-processed Al-3.5 RE alloy remains stable at 230 °C for 1 h due to micrometer- and nanometer-sized particles that pin the grain boundaries. Therefore, HPTE processing of Al-RE alloys has a high application potential in the electric power industry.

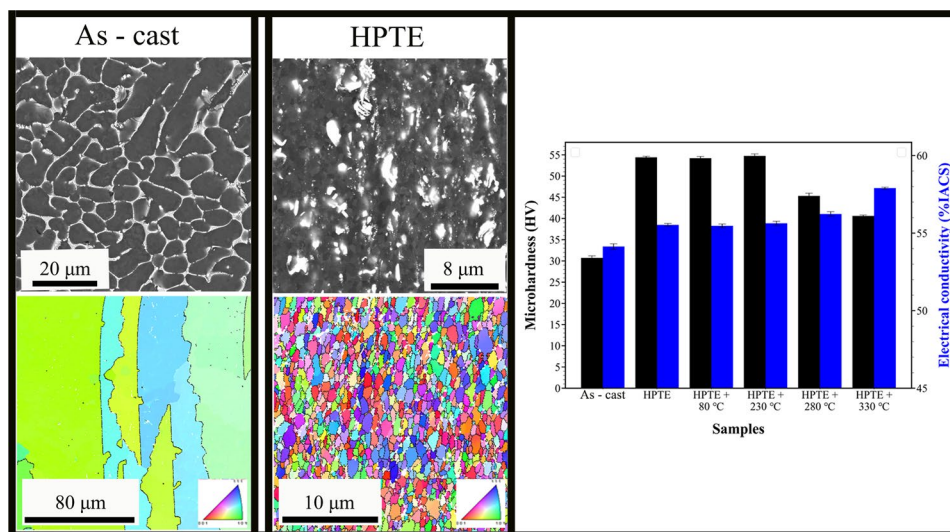
Handling Editor: Megumi Kawasaki.

Address correspondence to E-mail: yemao.lu@kit.edu; julia.ivanisenko@kit.edu

<https://doi.org/10.1007/s10853-024-09713-2>

Published online: 11 May 2024

GRAPHICAL ABSTRACT



Introduction

The electric power industry demands for materials with light weight, high strength, good electrical conductivity, and thermal stability continuously increasing [1, 2]. The Al-based alloys containing immiscible elements, such as Al–Zr, Al–Fe and Al–RE (where RE stands for rare earth) alloys, have gradually attracted the attention owing to their low density and their relatively high electrical conductivity and better thermal stability comparing with Al–Mg–Si electro-technical alloys [1, 3, 4]. The main issue of as-cast Al–Zr, Al–Fe, and Al–RE alloys, preventing their widespread use, is their low mechanical strength [4–7].

In order to overcome this drawback, processing using severe plastic deformation (SPD) has been proposed to enhance the mechanical properties of Al alloys [8]. It is well known that SPD techniques can refine grain sizes to the range of 100–1000 nm, which significantly enhances the strength according to the Hall–Petch relationship [9, 10]. For example, the tensile strength of aluminum alloys with different RE contents was significantly improved after HPT deformation at room temperature [11–13]. In particular, the tensile strength of the aluminum alloy with 4.5% RE increased from 80 to 489 MPa [11], and that of the aluminum alloy with 8.5% RE increased from 73 to 475 MPa [12]. However, the conductivity of the alloys decreased, respectively, from 55 to 45.5% and from 49.5 to 39.7% IACS [11, 12]. At the same time, the

application of the HPT process in the field of electric power is restricted due to several key issues: (i) the size limitation of the sample specimens, (ii) the continuous processing of samples is not possible, and (iii) the thermal stability of the UFG structure is limited.

High Pressure Torsion Extrusion (HPTE) (Fig. 1) is a novel SPD process, which can introduce very high strains in rods samples [14–17]. Omranpour et al. found that HPTE led to the formation of UFG microstructure in Al rods [16]. Nugmanov et al. used HPTE to process commercially pure copper by means of HPTE [17]. HPTE-processed copper has very high mechanical strength due to the presence of

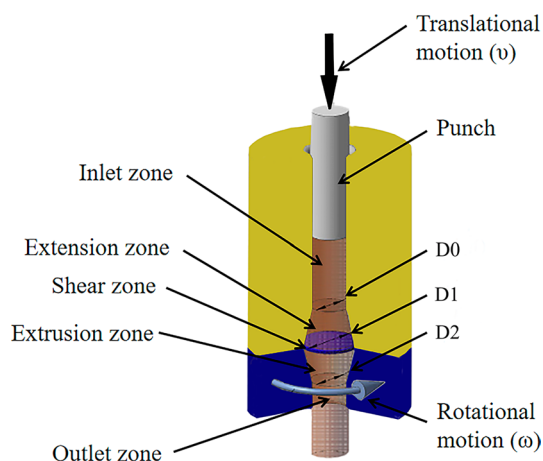


Figure 1 Schematic illustration of HPTE and the process parameters.

high density of high- and low-angle grain boundaries. However, to the best of our knowledge, there are no reports about the microstructure and properties of Al-based immiscible alloys using HPTE process.

In this paper, the HPTE is employed to process the rod samples of the Al–3.5 RE (2.2 wt.% cerium, 1.3 wt.% lanthanum) alloy at room temperature. The microstructure, mechanical properties, thermal stability, electrical conductivity, and their evolution at annealing of HPTE-deformed Al–3.5 RE alloy were systematically investigated. Meanwhile, the impact of microstructure on mechanical properties and electrical conductivity was analyzed through theoretical calculations. Finally, the discussion on the application potential of the HPTE-processed Al–3.5 RE alloy in the field of electrical engineering was conducted through comparison with the HPT process and the performance of the commercial 55KTAL alloy.

Materials and methods

As-cast Al–3.5% RE alloy rods with a diameter of 12 mm and a length of 35 mm were used for HPTE experiments. The HPTE deformation with translational velocity $v = 1$ mm/min and rotational velocity $\omega = 1$ rpm was carried out at room temperature using a custom-built computer-controlled HPTE machine (W. Klement GmbH, Lang, Austria) with advanced hexagon HPTE dies (Fig. 2). Molybdenum disulfide (MoS_2) was used as a lubricant in all experiments to facilitate the extrusion process. The HPTE equipment used in this study was described in Ref. [14]. Samples were extruded one by one through the die using

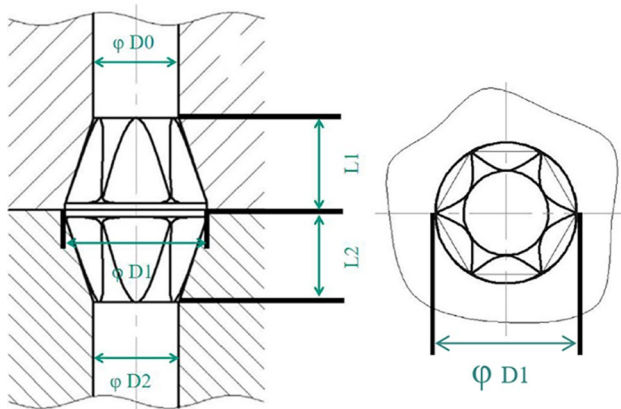


Figure 2 HPTE die drawing.

a punch moving with an extrusion speed v and lower die rotated with a rotational speed of ω . As a result, the specimens experienced both expansion-extrusion deformation and torsional deformation in a narrow zone where both dies meet. For one pass of HPTE, the equivalent strain is calculated by Equation [14]:

$$\epsilon_{HPTE} = 2\ln\frac{D1}{D0} + 2\ln\frac{D1}{D2} + \frac{2\pi\omega RD1}{\sqrt{3}vD2} \quad (1)$$

Following HPTE, samples were annealed in the temperature range from 80 to 330 °C for 1 h. Annealing treatments were carried out in a resistance-heated furnace in air atmosphere. For comparison, a few samples were processed by conventional HPT. Disks with a diameter of 10 mm and thickness of 0.6 mm were deformed at room temperature at a pressure of 5 GPa for five turns. The equivalent strain at HPT was calculated as:

$$\epsilon_{HPT} = \frac{2\pi NR}{\sqrt{3}t} \quad (2)$$

where N is the number of turns, t is the sample thickness, and R is the radial distance from the disk center.

The values of the equivalent strain at HPTE and HPT are listed in Table 1. The values reported in Table 1 are calculated using Eqs. (1) and (2).

The microhardness of samples was tested using a Vickers indenter. The electrical conductivity (EC, MS/m) was measured using eddy current electrical conductivity tester with an accuracy of $\pm 0.3\%$ in the longitudinal sample cross section (for details see SM). The following relation was used to express EC in International Annealed Copper Standard (IACS) units: $IACS = EC_{Al} / EC_{Cu} * 100$ [%], where EC_{Al} is the conductivity of the alloy in MS/m and EC_{Cu} is the conductivity of copper (58.0 MS/m). Tensile tests were conducted at ambient temperature using the Zwick Z100 testing machine and dog-bone samples with

Table 1 Equivalent strains at HPTE and HPT processing techniques calculated using Eqs. (1) and (2), respectively

Processing	Equivalent strain				
	R (mm)				
	0	1	2	3	4
HPTE	0.9	5.7	10.5	15.3	20.1
HPT	0	52.4	104.8	157.2	209.6

a diameter of 6.85 mm and gauge length of 15 mm shown in Fig. S2. The crystal structure of all samples was examined by X-ray diffraction (XRD) analysis using CuK α radiation at 40 kV and 40 mA. Values of lattice parameter a , coherent scattering domain size (CSDS), and microstrain $\langle \varepsilon^2 \rangle^{1/2}$ were calculated via the Rietveld refinement method using the Highscore software v. 5.1b by Malvern Panalytical and diffraction patterns shown in Fig. S3. The dislocation density (ρ_{\perp}) was calculated using the following equation [10]:

$$\rho_{\perp} = 2\sqrt{3} \langle \varepsilon^2 \rangle^{1/2} / (D \times b) \quad (3)$$

where b is the Burgers vector for gliding dislocations, D is the coherent scattering domain size, and $\langle \varepsilon^2 \rangle^{1/2}$ is a microstrain.

Microstructures were observed using several complementary techniques. The morphology of the second phase and the distribution of elements in initial sample, HPTE-processed specimen, and annealed HPTE-processed specimens were examined using a Zeiss Auriga 60 scanning electron microscope (SEM), operating at 20 kV, and employing backscattered electrons detector (BSE) and energy-dispersive X-ray spectroscopy (EDX) techniques.

The microstructure of the Al matrix of initial samples, HPTE-processed specimens, and annealed HPTE-processed specimens was investigated by electron backscattering diffraction (EBSD) using a Zeiss Auriga 60 and a FEI Quanta 3D scanning electron microscopes operating at 20 kV. EBSD samples were prepared by conventional electro-polishing procedure with a Tenupol twinjet polisher, using standard Struers solution for Al and further cleaned by ion milling (Gatan, PIPS II). The EBSD images were evaluated using the orientation imaging (OIM) software by EDAX.

The distribution of nanometer-scale intermetallic particles in the annealed HPTE-processed specimen was investigated by transmission electron microscopy (TEM), scanning transmission electron microscopy (STEM), and high-resolution TEM (HRTEM) techniques, employing a Themis 300 (ThermoFisher Scientific) electron microscope with a double aberration corrector operated at 300 kV. TEM samples were prepared by twin jet electro-polishing on Struers Tenupol using standard Struers solution for Al and further cleaned by ion milling (Gatan, PIPS II). HRTEM images were used to create associated Fast Fourier Transformation (FFT) patterns of the Al matrix and the second phase using Velox software v. 3.90 (ThermoFisher Scientific)

to study the structure and orientation of the region of interest.

Results

Mechanical strength, thermal stability, and electrical properties of Al–3.5 RE alloy after HPTE

The engineering stress–strain curves for the as-cast alloy, the HPTE-processed, and the annealed HPTE-processed sample are shown in Fig. 3a. The HPTE processing significantly increased the yield strength of the as-cast alloy from 126.9 ± 1.5 MPa to 224.9 ± 1.7 MPa. After the HPTE processing, the uniform elongation of the as-cast alloy decreased from 15 to 3.8%, and tensile curve demonstrated a kind of stress drop behavior. The high value of yield strength obtained after HPTE remains stable upon annealing at 230 °C. With an increase in the annealing temperature to 280 °C, the yield strength decreased to 192.4 ± 6.4 MPa. Remarkably, the stress-drop behavior became more pronounced after annealing (Fig. 3a), and possible reasons for that will be discussed below.

In order to study the thermal stability of the HPTE-processed alloy further, the microhardness measurements of the HPTE-processed and subsequently annealed samples were performed as shown in Fig. 3b. In the HPTE-processed sample, the microhardness increases along the radius of the transverse cross section from 47.5 to 60 Hv (Fig. 3b). This microhardness level remains stable after annealing in temperature range from 80 to 230 °C (Fig. 3b), in agreement with the behavior in yield strength. At further increase of annealing temperature, microhardness gradually decreases to 49 Hv at 280 °C and to 42 Hv at 330 °C, which is still higher than the microhardness of the as-cast alloy (Fig. 3b).

Figure 3c illustrates that the electrical conductivity of the as-cast alloy is $54.7 \pm 0.3\%$ IACS, which increases to $55.7 \pm 0.2\%$ IACS following the HPTE processing. Notably, the electrical conductivity of the HPTE-processed samples remains at that value after annealing in the temperature range from 80 to 230 °C (Fig. 3c). With increasing annealing temperature, the electrical conductivity exhibits a rather small increase, reaching $56.4 \pm 0.1\%$ IACS at 280 °C and $58.3 \pm 0.1\%$ IACS at 330 °C. Therefore, the optimal combination of high strength and high electric conductivity, achieved

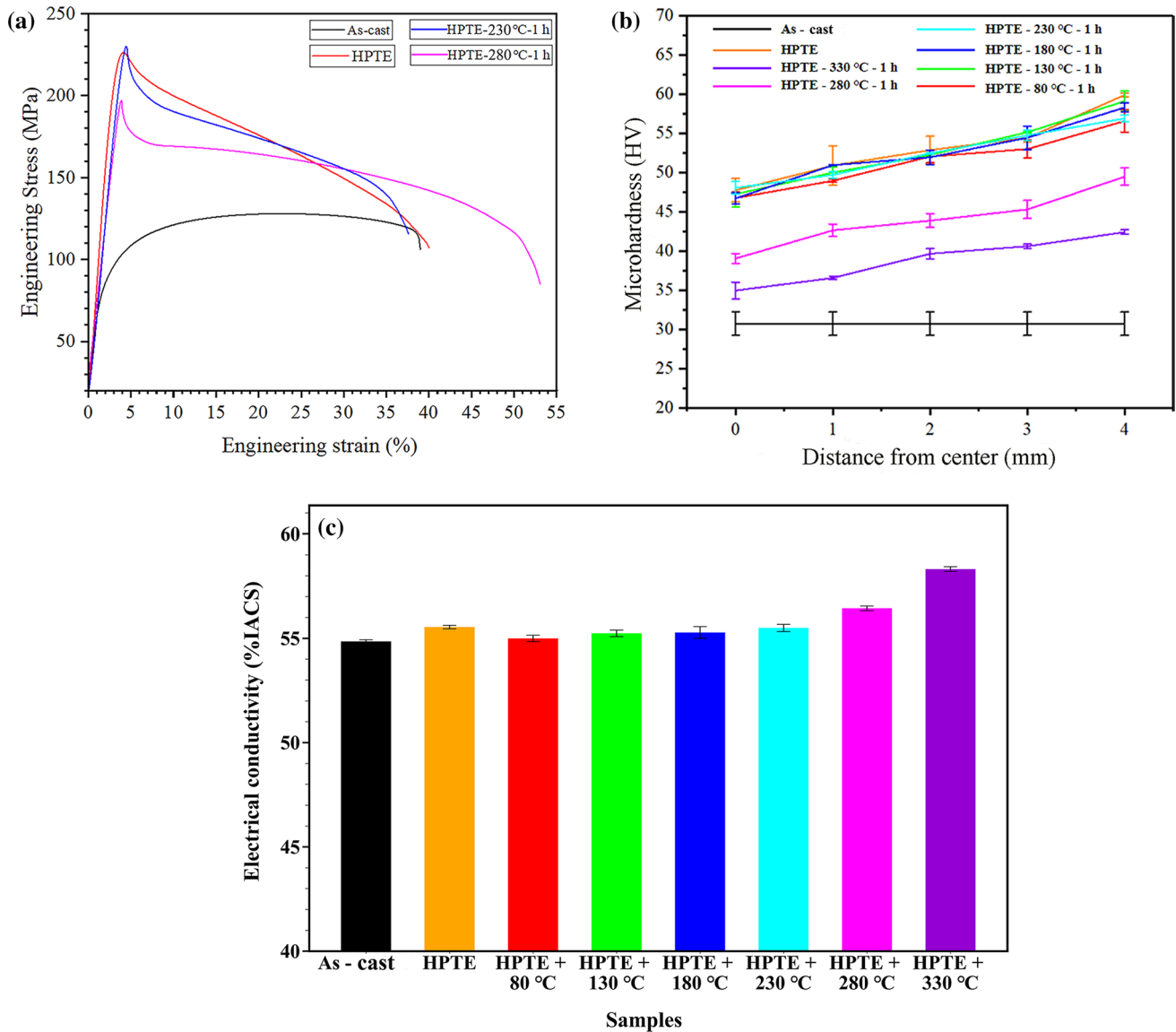


Figure 3 The engineering stress–strain curves of the as-cast alloy, the HPTE-processed sample, the HPTE-processed and annealed at 230 °C at 280 °C samples (a), Vickers microhardness

versus a distance from the center (b) and electrical conductivity (% IACS) of different samples in the longitudinal cross section of the rod (c).

through HPTE and subsequent annealing, is stable for annealing temperatures up to 230 °C.

Microstructure

Figure 4a shows the BSE-SEM image of the as-cast Al–3.5 RE alloy microstructure. The microstructure consists of an Al matrix with inclusions of the eutectic Al–RE intermetallic phase, which forms a continuous network with the size of the “cells” of 10–30 μm. The volume fraction of intermetallic

phase is $10.2 \pm 1.5\%$ in as-cast Al–3.5 RE alloy, as estimated from BSE–SEM images and in agreement with the phase diagram. The lamellar morphology of the intermetallic phase is illustrated in the insert in Fig. 4a. Figure 4b displays the EBSD orientation map of the initial sample. The mean grain size of the Al matrix in the initial sample is greater than 80 μm, which is substantially larger than the cell size of the $Al_{11}RE_3$ phase network. It means that the continuous network of the $Al_{11}RE_3$ phase is embedded into the Al matrix grains.

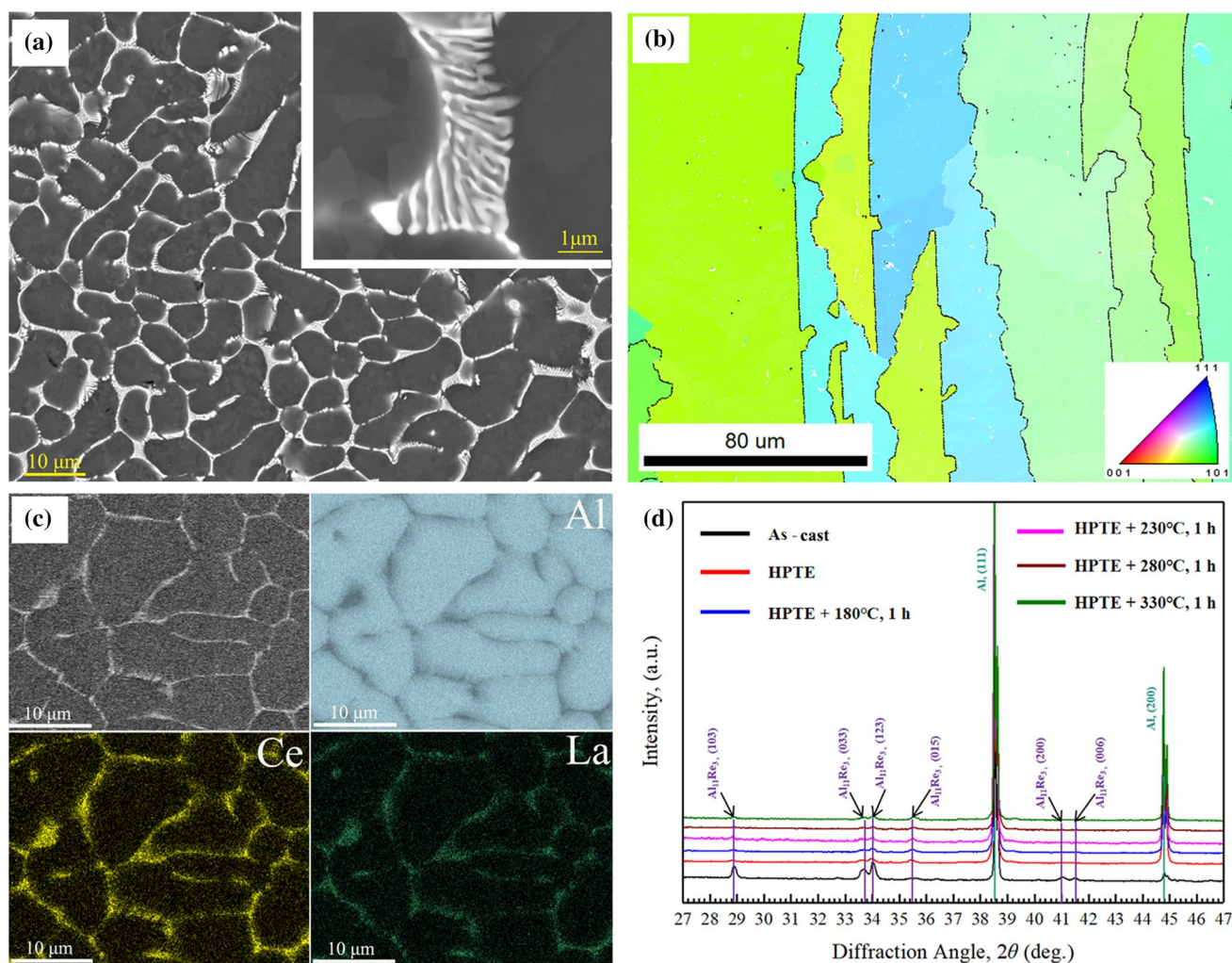


Figure 4 BSE—SEM image of the as-cast microstructure, insert shows the morphology of the $\text{Al}_{11}\text{RE}_3$ at higher magnification (a); EBSD orientation mapping of the as-cast sample (b); EDX

mapping of the as-cast sample (c); XRD patterns of the as-cast, the HPTE-processed and HPTE-processed and annealed samples (d).

The X-ray diffractogram of the as-cast alloy (Fig. 4d) contains the diffraction peaks of Al and the $\text{Al}_{11}\text{RE}_3$ intermetallic phase. After HPTE processing, the XRD peaks of $\text{Al}_{11}\text{RE}_3$ become significantly broader, which indicates a refinement of the $\text{Al}_{11}\text{RE}_3$ phase as a result of the HPTE processing [4]. EDX analysis of the initial sample showed that Ce and La are located in intermetallic particles but are not present in the Al matrix (Fig. 4c). This is reasonable since the solubility of Ce and La in Al at room temperature is negligible. However, it was reported that severe deformation by HPT had led to a partial decomposition of $\text{Al}_{11}\text{RE}_3$ intermetallic phase and dissolution of RE atoms in the Al matrix [11–13]. The results of the XRD analysis of Al–RE alloys, after HPTE and subsequent annealing,

are shown in Table 2. The lattice parameters of all samples are nearly identical, which suggests that the Ce and La atoms did not migrate into or out of the Al matrix during the HPTE and annealing processes, in agreement with the results of EDX analysis. The dislocation density of the HPTE-processed sample is rather high, remaining after annealing at 230 °C at the same level. However, upon further increasing the annealing temperature, the dislocation density decreased (Table 2).

Figure 5a–c shows the BSE—SEM images of the microstructure of the HPTE-processed sample at different locations in the normal cross section of the rod. In areas close to the rod axis where the equivalent strain is about 0.9, the morphology of the $\text{Al}_{11}\text{RE}_3$

Table 2 Microstructure data of Al-RE alloys after HPTE at RT and subsequent annealing

Sample	a (Å)	Grain size d_{av} (μm) (EBSD)	D (nm) (XRD)	$\langle \epsilon^2 \rangle^{1/2}$ (%)	ρ_{\perp} (m ⁻²)
as-cast	4.0499 ± 0.0001	> 80	–	–	–
HPTE	4.0496 ± 0.0001	0.9 ± 0.4	438 ± 11	0.050 ± 0.005	1.4 × 10 ¹³
HPTE + annealing 180 °C, 1 h	4.0496 ± 0.0001	–	434 ± 9	0.041 ± 0.004	1.1 × 10 ¹³
HPTE + annealing 230 °C, 1 h	4.0495 ± 0.0001	0.9 ± 0.5	439 ± 91	0.040 ± 0.004	1.1 × 10 ¹³
HPTE + annealing 280 °C, 1 h	4.0496 ± 0.0001	1.1 ± 0.5	636 ± 48	0.027 ± 0.009	5.1 × 10 ¹²
HPTE + annealing 330 °C, 1 h	4.0497 ± 0.0001	1.4 ± 0.6	811 ± 41	0.022 ± 0.005	1.9 × 10 ¹²

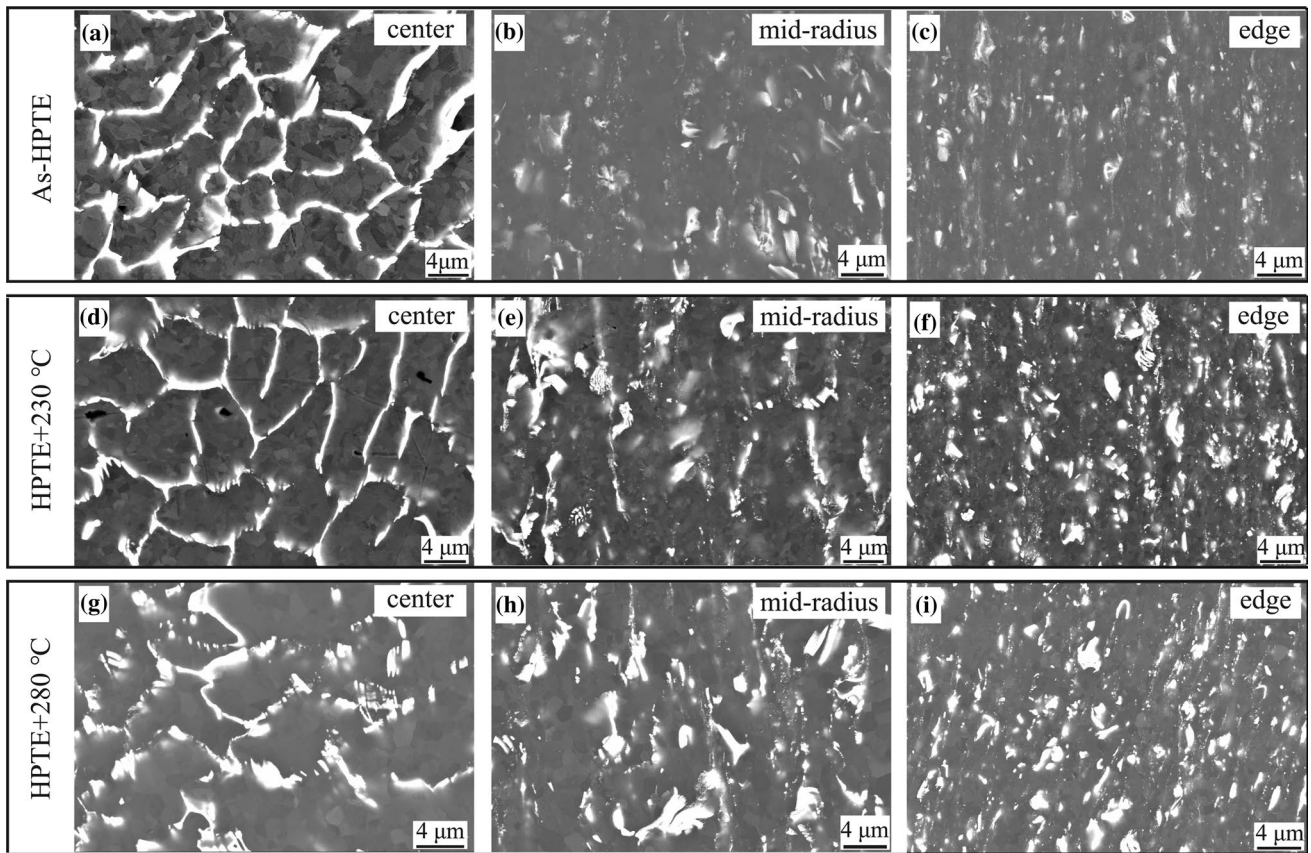


Figure 5 Microstructure of the HPTE-processed and subsequently annealed Al-3.5 RE samples at three different locations in the normal cross section of the rod: as-HPTE (a–c); HPTE and

annealed at 230 °C for 1 h (d–f); HPTE and annealed at 280 °C for 1 h (g–i). BSE-SEM.

phase still looks like a continuous network, similar to the morphology of this phase in the initial sample (Fig. 5a). At the middle of the radius where the equivalent strain is about 10.5, the continuous network of the

Al₁₁RE₃ phase is broken to micrometer and nanometer size particles (Fig. 5b). By increasing the equivalent strain to 20.1 at the HPTE rod edge, the size of the particles becomes smaller (Fig. 5c). The BSE-SEM

images of the HPTE-processed samples microstructure annealed at 230 and 280 °C for 1h are shown in (Fig. 5d–i). The microstructure looks very similar to that of the HPTE-processed sample.

Figure 6 shows the EBSD orientation maps in the normal cross section of the HPTE-processed Al–3.5 RE sample near the sample edge where the equivalent strain is 20.1 (Fig. 6a), and after annealing at 230, 280, and 330 °C (Fig. 5b–d). The mean grain size of the Al matrix in the HPTE-processed sample is about $0.9 \pm 0.4 \mu\text{m}$ (Fig. 6a) and does not change after annealing at 230 °C for 1 h (Fig. 6b). Increasing the annealing temperature to 280 °C for 1h results in a slight increase in the Al grain size to approximately $1.1 \pm 0.5 \mu\text{m}$ (Fig. 6c). This result demonstrates that the HPTE-processed sample has a good thermal stability in this temperature range, which is consistent with the microhardness measurements (Fig. 3b). A further increase in the annealing temperature to 330 °C for 1 h results in an increase in the Al grain size to $1.4 \pm 0.6 \mu\text{m}$ (Fig. 6d).

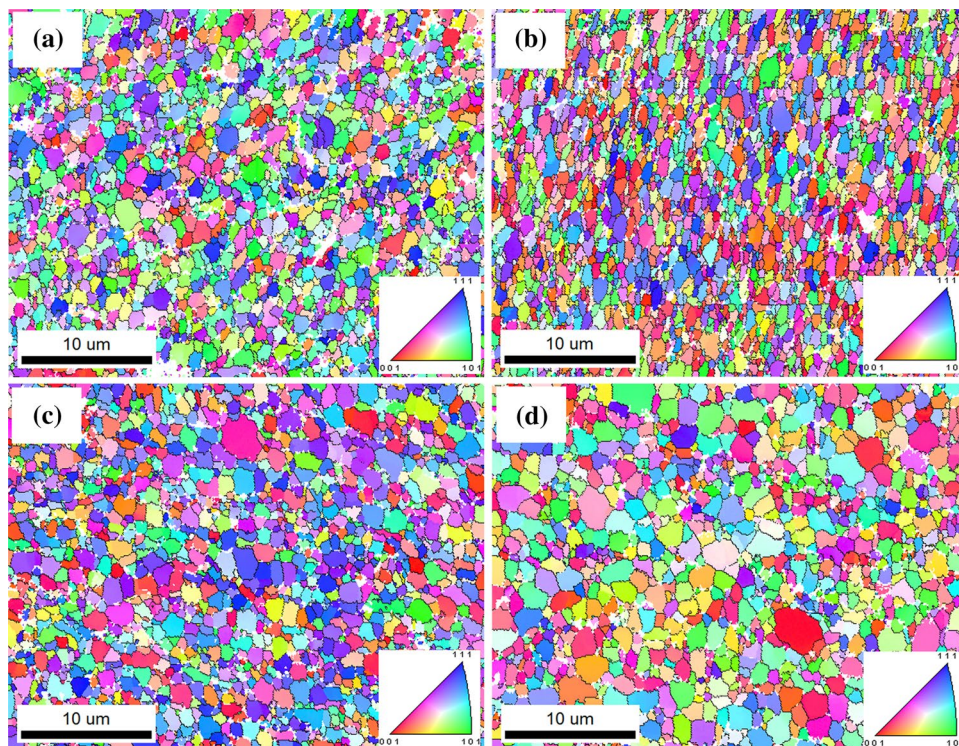
Figure 7 shows the STEM and STEM-EDX images in the normal cross section of the HPTE-processed sample annealed at 230 °C for 1 h near the sample edge (Fig. 7a). The STEM-EDX shows that Ce and La elements remain within the intermetallic particles and are not detected in the Al matrix (Fig. 7a), in agreement

with XRD data as deduced from the Al lattice parameter (Table 2). Moreover, micrometer- and nanometer-sized particles are clearly observed at one of the grain boundaries (Fig. 7a). TEM and HRTEM analysis of the HPTE-processed sample annealed at 230 °C for 1h reveals the nanometer-sized $\text{Al}_{11}\text{RE}_3$ phase particle pinned to the grain boundary (Fig. 7b, c).

Discussion

The trade-off between electrical conductivity and mechanical strength in aluminum alloys is well known [18]. The present research demonstrates that the HPTE process can simultaneously increase the yield strength, microhardness, and electrical conductivity of the Al–3.5 RE alloy rods compared to the values in the initial state (Fig. 3). The significant increase in yield strength and microhardness can be attributed to the transformation of the continuous network of the $\text{Al}_{11}\text{RE}_3$ phase into micrometer- and nanometer-sized particles (Fig. 5b, c), to the refinement of the Al matrix grain size from approx. 80 to $0.9 \mu\text{m}$ (Fig. 6a) and to the increased dislocation density (Table 2) as a result of HPTE processing. The presence of $\text{Al}_{11}\text{RE}_3$ phase can accelerate a refinement of the Al grains during HPTE process. It is well known that in alloys containing second phase

Figure 6 EBSD orientation maps of the microstructure of the Al–Re alloy: as-HPTE (a); HPTE and annealing at 230 °C (b); HPTE and annealing at 280 °C (c); HPTE and annealing at 330 °C (d).



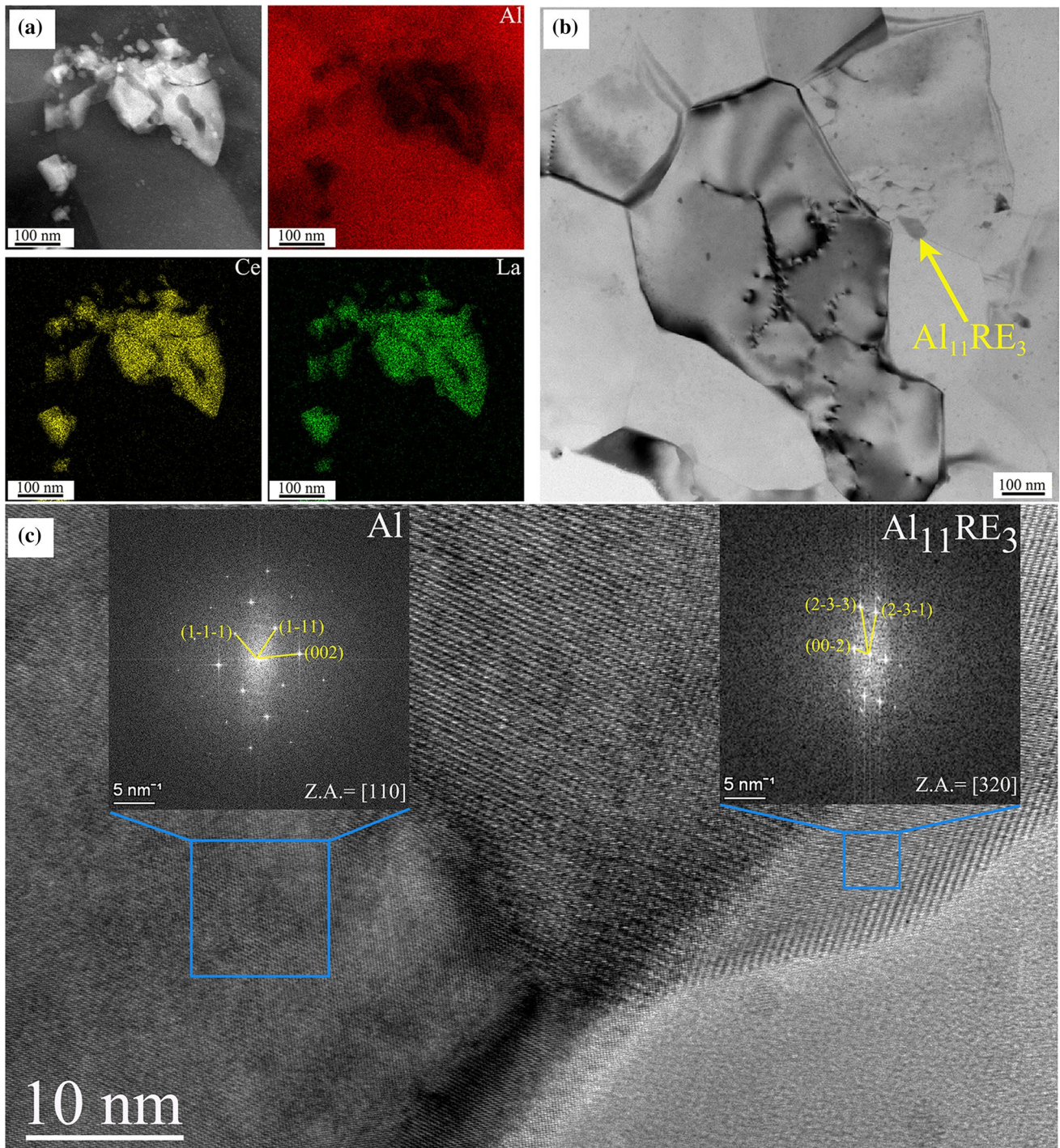


Figure 7 STEM-EDX mapping of the HPTE-processed Al-RE sample showing intermetallic particles (a); TEM micrograph (b) and HRTEM micrograph (c) of the HPTE-processed and

annealed at 230 °C sample. FFTs in (c) show zone axis of Al [110], and $Al_{11}RE_3$ [320].

particles, a relatively uniform submicron grain structure usually forms at significantly lower strain compared to that in the single-phase material [19]. Meanwhile, the

$Al_{11}RE_3$ phase effectively pins dislocations generated during HPTE processing thus leading to their storage in deformation zones in the Al matrix with significant

local misorientation gradients [20, 21]. Within these zones, new high-angle boundaries can emerge at relatively low strains [21]. Concurrently, the HPTE processing has a dual effect on electrical conductivity. On the one hand, it destroys the integrity of the intermetallic phase network, thus increasing the connectivity of the Al matrix (Fig. 5). The resistivity of intermetallic compounds is significantly higher than that of the matrix metal [22–24], and enhanced connectivity within the aluminum matrix facilitates an extended free path of conductive electrons. On the other hand, the decrease in grain size and increase in structural defects density due to severe deformation will lead to an increase in scattering centers for electrons and to a decrease in electrical conductivity [18]. The small observed changes of the electrical resistivity due to the HPTE processing and subsequent annealing indicate that the effects decreasing the electrical conductivity (grain size reduction, increased dislocation density) are in balance with the effects increasing the conductivity (destruction of connectivity of intermetallic). As a result, the resistivity is almost not altered, while the mechanical strength is improved substantially.

Strengthening mechanism

To illuminate the substantial enhancement of the strength of the Al–3.5 RE alloy after different treatments, a quantitative analysis based on microstructural parameters was conducted. The contribution of potential mechanisms to overall strengthening was estimated using the following general equation: [25, 26].

$$\sigma_{y0.2} = \sigma_0 + \sigma_{GB} + \sigma_{Dis} + \sigma_{Part} + \sigma_{ss} \quad (4)$$

Here, $\sigma_{y0.2}$ is the yield strength, σ_0 (10 MPa) is the Peierls–Nabarro stress [27] and σ_{GB} , σ_{Dis} , $\sigma_{(Pt)}$, and σ_{ss} are the strengthening contributions caused by grain boundaries, dislocations, nano meter intermetallic particles (≤ 100 nm), and solid solution, respectively.

The contribution of grain boundary strengthening can be described by the Hall–Petch relation, which is expressed as follows [10]:

$$\sigma_{GB} = \frac{k}{\sqrt{d_{av}}} \quad (5)$$

where k ($0.07 \text{ MPa}\cdot\text{m}^{-2}$) is the Hall–Petch coefficient [28], and d_{av} is the average grain size, estimated from EBSD orientation mapping (Table 2).

The contribution of dislocations to the strengthening can be estimated using the Bailey–Hirsch relationship [29]:

$$\sigma_{Dis} = M * \alpha * G * b * \sqrt{\rho_{\perp}} \quad (6)$$

In this equation, M (3.06) is the Taylor factor [29], α (0.33) is a dimensionless constant related to the dislocation interaction [29], G (26 GPa) is the shear modulus of Al [30], b (0.286 nm) is the Burgers vector [30], and ρ_{\perp} is the dislocation density, estimated from XRD results (Table 2).

The fragmentation leads to a progressive increase in the nano-meter intermetallic particle number density. So, the contribution of the nano-meter intermetallic particles (≤ 100 nm) to the strength can be given by the following equation through the Orowan mechanism [1, 31].

$$\sigma_{Part} = 0.7 * M * G * b * \frac{\sqrt{f_v}}{r} \quad (7)$$

In this equation, M , G , and b are the same as in Eq. (6), f_v is the volume fraction, and r is the mean radius of the nano-meter intermetallic particles.

The volume fraction of nanometer-size intermetallic particles was estimated using ImageJ software and several STEM images like shown in (Fig.S4). Upon that only particles with a diameter of ≤ 100 nm were analyzed. In that way, f_v was estimated as $6.2 \pm 0.6\%$ for the as-HPTE sample and $5.8 \pm 0.6\%$ for the annealed HPTE-processed sample. The mean radius of the nanometer intermetallic particles was measured as 45 nm for both the as-HPTE sample and the annealed HPTE-processed sample.

The solubility of La and Ce in Al at room temperature is less than 0.0005 wt.% [32], which is effectively zero. And from XRD results, the Al lattice parameters of all samples are nearly identical, which suggests that the Ce and La atoms did not migrate into or out of the Al matrix during the HPTE and annealing processes. Thus, the solid solution strengthening can be neglected.

A summary of the contributions of various strengthening mechanisms to the total yield strength is presented in Table 3 and compared with the experimental values. Theoretical calculations reveal that both grain boundary strengthening and the strengthening effect of nanometer-scale intermetallic particles play significant role in enhancing the yield strength of the Al–3.5 RE alloy. Grain boundary strengthening, as

Table 3 Strengthening by different mechanism in HPTE-processed and annealed at 280 °C Al-3.5RE alloy calculated using Eqs. (4–7) in comparison with experimentally measured yield strength

Sample	σ_0 (MPa)	σ_{GB} (MPa)	σ_{Dis} (MPa)	σ_{Part} (MPa)	σ_{ss} (MPa)	$\sigma_{y0.2}$ (MPa)	σ_{Exp} (MPa)
HPTE	10	80 ± 26	26	90	0	200 ± 26	224.9 ± 1.7
HPTE + annealing 280 °C, 1 h	10	73 ± 25	15	88	0	180 ± 25	192.4 ± 6.4

explained by the Hall–Petch relationship, occurs due to the impediment of dislocation motion by the grain boundaries, which becomes more pronounced as the grain size decreases. The nanometer intermetallic particles contribute to strengthening through Orowan strengthening, where these particles impede the movement of dislocations. After annealing at 280 °C for 1 h, the calculated yield strength of the HPTE-processed sample decreased. This reduction in strength is attributed to the increase in average grain size of the aluminum matrix from 0.9 μm to 1.1 μm and a decrease in dislocation density from 1.4×10^{13} to $5.1 \times 10^{12} \text{ m}^{-2}$.

Stress drop phenomena in the stress–strain curves

HPTE-processed ultrafine-grained Al–3.5RE alloy demonstrated an interesting feature in the strain–stress curves with a steep stress drop after a short uniform elongation stage of 3.8% (Fig. 3a). This behavior became more pronounced after annealing at 230 and 280 °C, as the alloy demonstrated a classic yield point with a flow stress drop just after the onset of yielding. A very similar behavior was observed in UFG Al processed by Accumulated Roll Bonding [33] and in cryomilled Al–Mg alloy [34–36]. Han et al. [34] argued that the most plausible explanation for this phenomenon is pinning of dislocations at disperse particles of secondary phases. A stress drop in the stress–strain curve can occur when dislocations either burst out from particles under high applied stresses or annihilate each other near these particles [34]. It is very likely that this mechanism is also active in the case of present investigation, because the alloy contains 10.18 vol. % of $\text{Al}_{11}\text{RE}_3$ intermetallic phase which had been broken into disperse particles after HPTE (Fig. 5). Different stress drop behavior of as-HPTE and annealed samples can be explained by different dislocation configurations in these states. Presumably, not all dislocations accumulated in the microstructure of the as-HPTE sample

were pinned at the $\text{Al}_{11}\text{RE}_3$ particles, which allowed some strain hardening before the pinned dislocations were released. After annealing at 230 °C and 280 °C, dislocation density was still very high, 1.1×10^{13} to $5.1 \times 10^{12} \text{ m}^{-2}$, respectively (Table 2); therefore, remaining “free” dislocations had not recovered but progressively pinned to the particles as exemplarily shown in Fig. 7b. Simultaneous release of such a huge number of dislocations at the yield point had led to a pronounced stress drop. More detailed investigations with the help of in situ TEM and other techniques, necessary to further clarify the mechanism of stress drop phenomenon in the ultrafine-grained Al–3.5% RE alloy, are over the scope of present investigation and should be performed in the future.

Electrical conductivity

The impact of various microstructural features on electrical resistivity can be quantitatively assessed by the Matthiessen’s rule [37].

$$\rho_{cal} = \rho_{pure} + \rho_{vac} + \rho_{Dis} + \rho_{GB} + \rho_{Pr} + \rho_{ss} \quad (8)$$

where ρ_{pure} (2.7 μΩ.cm) is the electrical resistivity of single-crystalline defect-free aluminum [38] and ρ_{vac} , ρ_{Dis} , ρ_{GB} , (ρ_{Pr}), and ρ_{ss} are the electrical resistivity contributions from vacancies, dislocations, grain boundaries, solute atoms and precipitation, respectively.

The contribution of vacancies to the electrical resistivity can be calculated using the following equation [39]

$$\rho_{vac} = N_{vac} * \Delta\rho^{Vac} \quad (9)$$

where N_{vac} (190 μΩ.cm) is vacancy concentration for severely deformed Al [39] and $\Delta\rho^{Vac}$ (10^{-4} to 10^{-3} μΩ.cm) is the resistivity per unit atomic concentration of vacancies [40]. The maximum contribution of vacancies to the electrical resistivity is as small as 0.2 μΩ.cm.

The contribution of dislocation density to the electrical resistivity can be calculated as [39]

$$\rho_{Dis} = \rho_{\perp} * \Delta\rho^{Dis} \quad (10)$$

where ρ_{\perp} is the dislocation density in m^{-2} and $\Delta\rho^{Dis}$ ($2.7 \times 10^{-25} \Omega m^3$) is the electrical resistivity per unit density of dislocations [41]. With the ρ_{\perp} values estimated from XRD results (Table 2), the contribution of dislocations to electrical resistivity is deemed negligible after HPTE and annealing.

The contribution of grain boundaries to the electrical resistivity can be estimated as follows [41]:

$$\rho_{GB} = S_{GB} * \Delta\rho^{GB} \quad (11)$$

Here, $S_{GB}(m^{-1}) \approx 3*d_{av}$ is the bulk density of grain boundaries in a material with an average grain size of d_{av} and $\Delta\rho^{GB}$ is the resistivity per unit concentration of grain boundaries which is $2.6 \times 10^{-16} \Omega m^2$ for Al [41].

The contribution from precipitates can be ignored because their contribution is not usually significant [4].

The contributions from solute atoms also can be ignored because no La, Ce atoms were detected within the Al matrix of all samples.

The results of the estimate of all contributions to electrical resistivity from different microstructural features are given in Table 4 and compared with the experimental data. The electrical conductivity in the international annealed copper standard (%IACS) was calculated as $K_{\%IACS} = 172.41/\rho$ [4], where ρ is the electrical resistivity in $\mu\Omega.cm$. Theoretical calculations indicate that the grain boundaries have the highest influence on electrical resistivity of the Al–3.5 RE alloy. After annealing at 280 °C for 1 h, the calculated electrical conductivity of the HPTE-processed sample increased due to the increase in grain size of the average aluminum matrix from 0.9 to 1.1 μm . The estimated values of electrical conductivity are in a good agreement with experimental ones.

Table 5 Comparison of microhardness and electric conductivity, measured at the middle of sample radius, of the Al-3.5 RE samples after different treatments

Processing	Microhardness, HV	Electrical conductivity, IACS, %
as-cast	31 ± 1.5	54.7 ± 0.3
HPTE	55 ± 0.6	55.7 ± 0.2
HPTE + 230 °C, 1 h	54 ± 0.5	56.4 ± 0.1
HPT	106 ± 8	47 ± 0.9
HPT + 230 °C, 1 h	126 ± 7	50.2 ± 0.7

Thermostability

The microhardness of the HPTE-processed rods of Al–3.5 RE alloy remains unchanged at annealing temperatures below 230 °C. The present results indicate that the thermal stability of the HPTE-processed Al–3.5 RE alloy is improved compared to that of many other SPD-processed Al alloys [42]. This can be attributed to the outstanding thermal stability of the $Al_{11}RE_3$ intermetallic phase [43] and the pinning effect of micrometer and nanometer $Al_{11}RE_3$ particles for Al grain boundary migration, which prevents grain coarsening, thus stabilizing the UFG structure. Further increase in the annealing temperature to 330 °C for 1 h results in a decrease in the microhardness of the HPTE-processed rods of Al–RE alloy to about 42 HV, while the electrical conductivity increases to about 58% IACS. This can be attributed to a significant increase in the grain size of the Al matrix (Table 2), which leads to a lowering the number of electron scattering centers.

Comparison of HPT and HPTE processing

The difference between HPT processing and HPTE processing was analyzed. Comparing the microhardness and electric conductivity of the Al–3.5 RE alloy after different treatments, it becomes evident that the microhardness of the alloy is higher after HPT

Table 4 Influence of different microstructural features on electrical resistivity calculated using Eqs. (8–11) in comparison with experimentally measured electrical conductivity

Sample	$\rho_{pure}(\mu\Omega.cm)$	$\rho_{vac}(\mu\Omega.cm)$	$\rho_{GB}(\mu\Omega.cm)$	$\rho_{Cal}(\mu\Omega.cm)$	% IACS _{Cal}	% IACS _{Exp}
HPTE	2.7	0.2	0.11 ± 0.07	3.02 ± 0.11	57.3 ± 1.8	55.7 ± 0.2
HPTE + annealing 280 °C, 1 h	2.7	0.2	0.09 ± 0.06	2.81 ± 0.08	57.7 ± 1.6	56.4 ± 0.1

processing than that after HPTE (Table 5). This result is not surprising taking into account the significantly higher strain realized in HPT compared to HPTE (Table 1). At the same time, the electrical conductivity of the HPTE-processed sample is higher than that of the HPT-processed one (Table 5). It is not the purpose of the present letter to analyze the reasons for such a large difference in properties of HPT and HPTE-processed Al-3.5 RE alloy. It can be speculated that HPT leads not only to stronger grain size refinement, but also to the partial dissolution of the intermetallic phase and formation of a supersaturated solid solution in Al as demonstrated previously in the HPT-processed Al-RE alloys [11–13], which would be detrimental for the electrical conductivity. A notable increase in hardness of the HPT-processed and annealed at 230 °C sample was explained in [11–13] by the precipitation of $Al_{11}RE_3$ nanoparticles from the super-saturated solid solution (age hardening). Irrespective of that, the HPT-processed samples show the usual strength vs. electric conductivity trade-off, whereas HPTE-processed samples show a simultaneous enhancement of both characteristics. After annealing at 230 °C for 1 h, the microhardness of the HPTE Al-3.5 RE is still lower, but its electrical conductivity is notably higher than the value of the HPT-processed sample. Anyway, HPT processing is a laboratory-scale processing method and up to now it has never been used in industry.

Comparison of commercial 55KTAL and HPTE-processed Al-3.5 RE alloy

The electrical conductivity and tensile strength of the HPTE-processed Al-3.5 RE alloy are similar to that of a commercial Al-Zr-Si-Cu-thermal-resistant aluminum alloy for high-tension conductors 55KTAL [44] (Table 6). However, its ductility and thermal stability are significantly better than that of the 55KTAL alloy. It should be noted that the properties of the HPTE-Al-3.5 RE alloy remained stable when exposed to a temperature of 230 °C for one hour, which is equivalent to maintaining tensile strength over a thermal history of 36 years at an operational temperature of 150 °C for conductors [44]. Additionally, the proposed processing method by HPTE of the Al-3.5 RE alloy is rather simple and involves a single deformation step, in contrast with the multi-stage procedure used in industry for the 55KTAL alloy, including rolling, wire drawing, time- and energy-consuming aging treatment, and one more

Table 6 Mechanical properties and electric conductivity of a commercial 55KTAL alloy [44] and Al-3.5 RE alloy processed by HPTE

Alloy type	Properties	
	55KTAL [27]	HPTE-Al-3.5 RE
Wire diameter (mm)	4.8	6.8
Conductivity (% IACS)	55	55.7
Tensile strength (MPa)	225	226
Elongation (%)	2.0	3.8
Thermal stability (°C)	180	230

wire drawing [44]. In terms of potential for industrial applications, in addition to the favorable property combination identified in this work, it should be emphasized that HPTE processing yields rods samples, in contrast, for example, with HPT. Furthermore, in a combination with Conform™ process, HPTE allows production of rods or wires with any desirable length [45].

Conclusions

In summary, a new severe plastic deformation process, High Pressure Torsion Extrusion, has been successfully used to process rod-shaped samples of aluminum rare earth alloy Al-3.5 at. % (La, Ce). Our research indicates that HPTE processing can effectively reduce the size of the Al grains and destroy the continuous network of intermetallic phase in a single pass at room temperature, resulting in a simultaneous increase in mechanical strength and electrical conductivity. During annealing at temperatures below 230 °C, the microstructure and microhardness of the HPTE-processed Al-3.5 RE alloy rods remain stable, while the electrical conductivity increases to about 55% IACS. HPTE meets the requirements of continuous processing technology, and the deformed Al-3.5 RE alloy exhibits good mechanical properties, electrical conductivity, and thermal stability. That indicates tremendous potential for applications of HPTE in electrical engineering, especially for high-voltage transmission. This study also provides a novel approach for designing Al-alloys with high mechanical properties, good electrical conductivity, and thermal stability.

Acknowledgements

This work was partially supported by China Scholarship Council [Grant No. 202006670001]. The authors gratefully acknowledge Karlsruhe Nano Micro Facility (KNMFi, www.knmf.kit.edu) for providing advanced characterization techniques. This work was partly carried out with the support of the Joint Laboratory Model and Data-driven Materials Characterization (JL MDMC), a cross-center platform of the Helmholtz Association. Thanks to Jung Soo for the assistance with samples preparation. We are gratefully indebted to Dr. R. Kruk for valuable discussions and Dr. M. Murashkin for providing alloy samples.

Author contributions

RX involved in methodology, investigation, data curation, data analysis, writing—original draft, writing—review and editing. YL took part in methodology, data analysis, writing—review and editing. YD involved in data analysis, writing—review. AB involved in data analysis, writing—review. HH took part in writing—review and editing. YI involved in supervision, conceptualization, methodology, writing—review and editing.

Funding

Open Access funding enabled and organized by Projekt DEAL.

Data availability

The raw data required to reproduce these findings are available on request.

Declarations

Conflict of interest The authors declare that they have no conflict of interest.

Ethical approval Not applicable, as no experiments utilizing human tissue were performed in this study.

Supplementary Information The online version contains supplementary material available at <https://doi.org/10.1007/s10853-024-09713-2>.

Open Access This article is licensed under a Creative Commons Attribution 4.0 International License, which permits use, sharing, adaptation, distribution and reproduction in any medium or format, as long as you give appropriate credit to the original author(s) and the source, provide a link to the Creative Commons licence, and indicate if changes were made. The images or other third party material in this article are included in the article's Creative Commons licence, unless indicated otherwise in a credit line to the material. If material is not included in the article's Creative Commons licence and your intended use is not permitted by statutory regulation or exceeds the permitted use, you will need to obtain permission directly from the copyright holder. To view a copy of this licence, visit <http://creativecommons.org/licenses/by/4.0/>.

References

- [1] Duchaussoy A, Sauvage X, Edalati K et al (2019) Structure and mechanical behavior of ultrafine-grained aluminum-iron alloy stabilized by nanoscaled intermetallic particles. *Acta Mater* 167:89–102. <https://doi.org/10.1016/j.actamat.2019.01.027>
- [2] Sauvage X, Bobruk EV, Murashkin MY et al (2015) Optimization of electrical conductivity and strength combination by structure design at the nanoscale in Al–Mg–Si alloys. *Acta Mater* 98:355–366. <https://doi.org/10.1016/j.actamat.2015.07.039>
- [3] Light metals 2013. Springer, 2017.
- [4] Mohammadi A, Enikeev NA, Murashkin MY et al (2021) Developing age-hardenable Al–Zr alloy by ultra-severe plastic deformation: Significance of supersaturation, segregation and precipitation on hardening and electrical conductivity. *Acta Mater* 203:116503. <https://doi.org/10.1016/j.actamat.2020.116503>
- [5] Cubero-Sesin JM, Horita Z (2015) Age hardening in ultrafine-grained Al-2 pct Fe alloy processed by high-pressure torsion. *Metall Mater Trans A* 46:2614–2624. <https://doi.org/10.1007/s11661-015-2876-6>
- [6] Rogachev SO, Naumova EA, Lukina EA et al (2021) High strength al–la, al–ce, and al–ni eutectic aluminum alloys

- obtained by high-pressure torsion. *Materials* 14(21):6404. <https://doi.org/10.3390/ma14216404>
- [7] Rogachev SO, Naumova EA, Vasileva ES et al (2022) Al–Ca, Al–Ce, and Al–La eutectic aluminum alloys processed by high-pressure torsion. *Adv Eng Mater* 24(2):2100772. <https://doi.org/10.1002/adem.202100772>
- [8] Edalati K, Bachmaier A, Beloshenko VA et al (2022) Nanomaterials by severe plastic deformation: review of historical developments and recent advances. *Mater Res Lett* 10(4):163–256. <https://doi.org/10.1080/21663831.2022.2029779>
- [9] Valiev RZ, Enikeev NA, Murashkin MY et al (2010) On the origin of the extremely high strength of ultrafine-grained Al alloys produced by severe plastic deformation. *Scr Mater* 63(9):949–952. <https://doi.org/10.1016/j.scriptamat.2010.07.014>
- [10] Pande CS, Cooper KP (2009) Nanomechanics of Hall–Petch relationship in nanocrystalline materials. *Prog Mater Sci* 54(6):689–706. <https://doi.org/10.1016/j.pmatsci.2009.03.008>
- [11] Murashkin MY, Sabirov I, Medvedev AE et al (2016) Mechanical and electrical properties of an ultrafine grained Al–8.5 wt.% RE (RE = 5.4 wt.% Ce, 3.1 wt.% La) alloy processed by severe plastic deformation. *Mater Design* 90:433–442. <https://doi.org/10.1016/j.matdes.2015.10.163>
- [12] Medvedev AE, Murashkin MY, Enikeev NA et al (2019) Effect of the eutectic Al–(Ce, La) phase morphology on microstructure, mechanical properties, electrical conductivity and heat resistance of Al–45 (Ce, La) alloy after SPD and subsequent annealing. *J Alloys Compd* 796:321–330. <https://doi.org/10.1016/j.jallcom.2019.05.006>
- [13] Medvedev AE, Murashkin MY, Enikeev NA et al (2018) Enhancement of mechanical and electrical properties of Al–RE alloys by optimizing rare-earth concentration and thermo-mechanical treatment. *J Alloys Compd* 745:696–704. <https://doi.org/10.1016/j.jallcom.2018.02.247>
- [14] Ivanisenko Y, Kulagin R, Fedorov V et al (2016) High pressure torsion extrusion as a new severe plastic deformation process. *Mater Sci Eng A* 664:247–256. <https://doi.org/10.1016/j.msea.2016.04.008>
- [15] Kulagin R, Beygelzimer Y, Estrin Y et al (2019) A mathematical model of deformation under high pressure torsion extrusion. *Metals* 9(3):306. <https://doi.org/10.3390/met9030306>
- [16] Omranpour B, Ivanisenko Y, Kulagin R et al (2019) Evolution of microstructure and hardness in aluminum processed by High Pressure Torsion Extrusion. *Mater Sci Eng, A* 762:138074. <https://doi.org/10.1016/j.msea.2019.138074>
- [17] Nugmanov D, Mazilkin A, Hahn H et al (2019) Structure and tensile strength of pure Cu after high pressure torsion extrusion. *Metals* 9(10):1081. <https://doi.org/10.3390/met9101081>
- [18] Valiev RZ, Murashkin MY, Sabirov I (2014) A nanostructural design to produce high-strength Al alloys with enhanced electrical conductivity. *Scr Mater* 76:13–16. <https://doi.org/10.1016/j.scriptamat.2013.12.002>
- [19] Apps PJ, Bowen JR, Prangnell PB (2003) The effect of coarse second-phase particles on the rate of grain refinement during severe deformation processing. *Acta Mater* 51(10):2811–2822. [https://doi.org/10.1016/S1359-6454\(03\)00086-7](https://doi.org/10.1016/S1359-6454(03)00086-7)
- [20] Humphreys FJ, Hatherly M (2012) *Recrystallization and related annealing phenomena*. Elsevier, Amsterdam
- [21] Humphreys FJ, Kalu PN (1990) The plasticity of particle-containing polycrystals. *Acta Metall Mater* 38(6):917–930. [https://doi.org/10.1016/0956-7151\(90\)90164-C](https://doi.org/10.1016/0956-7151(90)90164-C)
- [22] Cao M, Luo Y, Xie Y et al (2019) The influence of interface structure on the electrical conductivity of graphene embedded in aluminum matrix. *Adv Mater Interfaces* 6(13):1900468. <https://doi.org/10.1002/admi.201900468>
- [23] Gao W, Sammes NM (1999) *An introduction to electronic and ionic materials*. World Scientific, Singapore
- [24] Kasap SO (2006) *Electronic materials and Devices*. McGraw-Hill, New York
- [25] Kamikawa N, Huang X, Tsuji N et al (2009) Strengthening mechanisms in nanostructured high-purity aluminium deformed to high strain and annealed. *Acta Mater* 57(14):4198–4208. <https://doi.org/10.1016/j.actamat.2009.05.017>
- [26] Wen H, Topping TD, Isheim D et al (2013) Strengthening mechanisms in a high-strength bulk nanostructured Cu–Zn–Al alloy processed via cryomilling and spark plasma sintering. *Acta Mater* 61(8):2769–2782. <https://doi.org/10.1016/j.actamat.2012.09.036>
- [27] Totten GE, MacKenzie DS (2003) *Handbook of aluminium, physical metallurgy and processes, vol 1*. CRC Press, Boca Raton
- [28] Witkin DB, Lavernia EJ (2006) Synthesis and mechanical behavior of nanostructured materials via cryomilling. *Prog Mater Sci* 51(1):1–60. <https://doi.org/10.1016/j.pmatsci.2005.04.004>
- [29] Hansen N, Huang X (1998) Microstructure and flow stress of polycrystals and single crystals. *Acta Mater* 46(5):1827–1836. [https://doi.org/10.1016/S1359-6454\(97\)00365-0](https://doi.org/10.1016/S1359-6454(97)00365-0)
- [30] Edalati K, Akama D, Nishio A et al (2014) Influence of dislocation–solute atom interactions and stacking fault energy on grain size of single-phase alloys after severe plastic deformation using high-pressure torsion. *Acta*

- Mater 69:68–77. <https://doi.org/10.1016/j.actamat.2014.01.036>
- [31] Han BQ, Mohamed FA, Lavernia EJ (2003) Tensile behavior of bulk nanostructured and ultrafine grained aluminum alloys. *J Mater Sci* 38:3319–3324. <https://doi.org/10.1023/A:1025150407956>
- [32] Henderson HB, Hammons JA, Baker AA et al (2021) Enhanced thermal coarsening resistance in a nanostructured aluminium–cerium alloy produced by additive manufacturing. *Mater Des* 209:109988. <https://doi.org/10.1016/j.matdes.2021.109988>
- [33] Tsuji N, Ito Y, Saito Y et al (2002) Strength and ductility of ultrafine grained aluminum and iron produced by ARB and annealing. *Scripta Mater* 47(12):893–899. [https://doi.org/10.1016/S1359-6462\(02\)00282-8](https://doi.org/10.1016/S1359-6462(02)00282-8)
- [34] Han BO, Mohamed FA, Lee Z et al (2003) Mechanical properties of an ultrafine-grained Al-7.5 Pct Mg alloy. *Metall Mater Trans A* 34:603–613. <https://doi.org/10.1007/s11661-003-0095-z>
- [35] Han BQ, Lavernia EJ (2005) Deformation mechanisms of nanostructured Al alloys. *Adv Eng Mater* 7(6):457–465. <https://doi.org/10.1002/adem.200400219>
- [36] Han BO, Lavernia EJ, Lee Z et al (2005) Deformation behavior of bimodal nanostructured 5083 Al alloys. *Metall and Mater Trans A* 36:957–965. <https://doi.org/10.1007/s11661-005-0289-7>
- [37] Laik A, Bhanumurthy K, Kale GB (2004) Intermetallics in the Zr–Al diffusion zone. *Intermetallics* 12(1):69–74. <https://doi.org/10.1016/j.intermet.2003.09.002>
- [38] Fickett FR (1971) Aluminum—1. A review of resistive mechanisms in aluminum. *Cryogenics* 11(5):349–367. [https://doi.org/10.1016/0011-2275\(71\)90036-1](https://doi.org/10.1016/0011-2275(71)90036-1)
- [39] Setman D, Schafler E, Korznikova E et al (2008) The presence and nature of vacancy type defects in nanometals detained by severe plastic deformation. *Mater Sci Eng, A* 493(1–2):116–122. <https://doi.org/10.1016/j.msea.2007.06.093>
- [40] Khellaf A, Seeger A, Emrick RM (2002) Quenching studies of lattice vacancies in high-purity aluminium. *Mater Trans* 43(2):186–198. <https://doi.org/10.2320/matertrans.43.186>
- [41] Karolik AS, Luhvich AA (1994) Calculation of electrical resistivity produced by dislocations and grain boundaries in metals. *J Phys Condens Matter* 6(4):873. <https://doi.org/10.1088/0953-8984/6/4/007>
- [42] Horita Z, Fujinami T, Nemoto M et al (2000) Equal-channel angular pressing of commercial aluminum alloys: grain refinement, thermal stability and tensile properties. *Metall Mater Trans A* 31:691–701. <https://doi.org/10.1007/s11661-000-0011-8>
- [43] Zhang X, Li L, Wang Z et al (2023) Ultrafine-grained Al–La–Mg–Mn alloy with superior thermal stability and strength-ductility synergy. *Mater Sci Eng, A* 873:145035. <https://doi.org/10.1016/j.msea.2023.145035>
- [44] Ogawa T, Watabe M, Nakagawa H et al (2022) High-strength thermal-resistant aluminum alloy wire with improved conductivity and new conductor design. *Sumitomo Electr Tech Rev* 94:53–57
- [45] Hu J, Kulagin R, Ivanisenko Y et al (2020) Finite element modeling of Conform-HPTE process for a continuous severe plastic deformation path. *J Manuf Process* 55:373–380. <https://doi.org/10.1016/j.jmapro.2020.04.052>

Publisher's Note Springer Nature remains neutral with regard to jurisdictional claims in published maps and institutional affiliations.